

In Situ Characterizations Revealing Ruthenium-Atom-Induced Raise of Photocatalytic Performance

Amin Talebian-Kiakalaieh, Meijun Guo, Elhussein M. Hashem, Bingquan Xia, Yunling Jiang, Clarence Chuah, Youhong Tang, Philip Kwong, Jingrun Ran,* and Shi-Zhang Qiao*

Rational design/fabrication of high-activity photocatalysts is of central importance to realize solar-to-chemical conversion for tackling worldwide energy/environmental issues. Hence, it is desirable to disclose the element/space/time-resolved charge kinetics and surface species evolution of photocatalysts under realistic conditions using various in situ characterizations. Furthermore, the correlation of the above-disclosed mechanisms with atomic-scale compositions/structures of photocatalysts can further direct the atomic-level design/synthesis of high-performance photocatalysts. Herein, Ru atoms incorporated CdS quantum dots (QDs) are synthesized using an in situ hot-injection route. The optimized Ru incorporated CdS QDs (Ru0.1) exhibit excellent photocatalytic evolution rates of H_2O_2 ($8.78 \text{ mmol g}^{-1} \text{ h}^{-1}$) and benzaldehyde ($11.70 \text{ mmol g}^{-1} \text{ h}^{-1}$), respectively. Four different in situ characterizations demonstrate that in realistic conditions, the incorporated Ru atoms with high oxidation state (+3) effectively attract photo-generated electrons from bulk to the overall surface of Ru0.1; these directed electron flows also greatly facilitate the transfer of photo-generated holes from bulk to surface of Ru0.1 via efficiently reducing electron-hole recombination. In situ diffuse reflectance infrared Fourier transform spectroscopy, electron spin spectroscopy, and species-trapping experiments further reveal three possible reaction pathways for H_2O_2 evolution. This work underscores the use of in situ characterizations to reveal the element/space/time-resolved electrons/holes kinetics and surface-species generation for photocatalysts in realistic conditions.

1. Introduction

The conversion of renewable solar energy into clean fuels and valuable chemicals via photocatalysis is of significant importance to solve the global energy/environment issues. Rational design/synthesis of high-performance/cost-effective photocatalysts requires an insightful/comprehensive understanding on the kinetics of photo-generated electrons/holes in catalysts under realistic reaction conditions, e.g., light illumination, certain atmospheres, and reactants.^[1–9] Hence, the combination of various advanced in situ characterization techniques to provide the element/space/time-resolved information on the kinetics of photo-generated electrons and holes, respectively, in catalysts under realistic conditions is of great interest, but rarely reported.^[10] Furthermore, the correlation of electrons/holes kinetics revealed in realistic conditions and atomic-level structures/compositions for photocatalysts can further guide the

A. Talebian-Kiakalaieh, M. Guo, E. M. Hashem, B. Xia, Y. Jiang, P. Kwong, J. Ran, S.-Z. Qiao
School of Chemical Engineering
University of Adelaide
Adelaide, South Australia 5005, Australia
E-mail: jingrun.ran@adelaide.edu.au; s.qiao@adelaide.edu.au

C. Chuah, Y. Tang
Flinders Institute for NanoScale Science and Technology
College of Science and Engineering
Flinders University
Adelaide, South Australia 5042, Australia

 The ORCID identification number(s) for the author(s) of this article can be found under <https://doi.org/10.1002/aenm.202301594>

© 2023 The Authors. Advanced Energy Materials published by Wiley-VCH GmbH. This is an open access article under the terms of the Creative Commons Attribution-NonCommercial License, which permits use, distribution and reproduction in any medium, provided the original work is properly cited and is not used for commercial purposes.

DOI: 10.1002/aenm.202301594

atomic-scale design and synthesis of high-performance photocatalysts for desired reactions.^[11,12]

Hydrogen peroxide (H_2O_2) serves as an important green oxidant widely applied in pulp manufacturing, wastewater treatment, disinfection, and chemical synthesis.^[13–15] Besides, it is also a clean, storable, and transportable liquid fuel with an energy density of 3.0 MJ L^{-1} (60% H_2O_2), higher than that (2.8 MJ L^{-1}) of compressed H_2 gas at 35 MPa. Nevertheless, it is currently produced by the energy-consuming and waste-intensive anthraquinone route.^[16,17] Hence, it is of great significance to adopt the clean/environmentally-benign photocatalysis technique for the simultaneous generation of H_2O_2 and value-added chemicals, via efficiently using both the photo-generated electrons and holes in redox reactions.^[18–23]

Herein, Ruthenium (Ru) atoms incorporated CdS quantum dots (QDs) were designed and synthesized by an in situ hot-injection route. Ru (0.1 wt%) incorporated CdS QDs (Ru0.1) exhibits the highest activity of H_2O_2 evolution ($8.78 \text{ mmol g}^{-1} \text{ h}^{-1}$) with the largest enhancement factor of $\approx 1372\%$ compared to CdS QDs (Ru0). Ru0.1 also exhibits $\approx 168\%$ times higher averaged benzaldehyde (BAD) evolution rate ($11.70 \text{ mmol g}^{-1} \text{ h}^{-1}$) compared to Ru0 ($6.96 \text{ mmol g}^{-1} \text{ h}^{-1}$). Four different (quasi) in situ characterizations [i.e., quasi in situ X-Ray photoelectron spectroscopy (XPS), in situ atomic force microscopy-Kelvin probe force microscopy (AFM-KPFM), in situ transient-state surface photovoltage (SPV) spectroscopy, and in situ transient absorption spectroscopy (TAS)] reveal that in realistic conditions the incorporated Ru atoms with high oxidation state (+3) can not only strongly attract photo-generated electrons transferring from bulk to the overall surface of Ru0.1, but also obviously boost more photo-generated holes migrating to surface via restraining their recombination with electrons. In situ transient-state SPV spectroscopy discloses that the strong electron scavenger, oxygen (O_2), can efficiently capture the majority of photo-generated electrons on the surface in $\approx 0.1 \mu\text{s}$; the remaining photo-generated holes are approximately ten times more than those of Ru0. And in situ TAS reveals that in realistic conditions Ru0.1 can still retain $\approx 16\%$ photo-generated electrons at $\approx 3100 \text{ ps}$ after light excitation; while Ru0 can only reserve $\approx 8\%$ photo-generated electrons at the same time. Furthermore, in situ diffuse reflectance infrared Fourier transform spectroscopy (DRIFTS) confirms the generation of H_2O_2 and BAD for Ru0.1 in realistic conditions. The electron spin resonance (ESR) experiments combined with species-trapping experiments further confirm the three different reaction pathways for H_2O_2 evolution. This work highlights the significance of in situ characterizations revealing the element/space/time-resolved information on charge kinetics and surface-species evolution in realistic conditions to guide the atomic-scale design/synthesis of high-performance photocatalysts for key reactions.

2. Results and Discussion

2.1. Structure, Composition, and Electronic State

A range of Ruthenium (Ru) atoms incorporated monodispersed CdS quantum dots (QDs) were synthesized using an in situ hot-injection route. Ru atoms were in situ incorporated into the crystal structure of CdS QDs using Ruthenium (III) chloride (RuCl_3),

cadmium chloride (CdCl_2), and thioacetamide (TAA) as the precursors and oleylamine as the stabilizer. The as-synthesized samples are denoted as Ru0.05, Ru0.1, and Ru0.2, respectively, based on the nominal weight ratios (0.05, 0.1, and 0.2 wt%) of Ru in CdS QDs. Bare CdS QDs are annotated as Ru0. All the synthesis details are recorded in Supporting Information. The transmission electron microscopy (TEM) image (Figure S1a, Supporting Information) and atomic-resolution high angle annular dark field-scanning transmission electron microscopy (HAADF-STEM) images of Ru0 (Figure S1b,c, Supporting Information) and energy dispersive X-ray spectroscopy (EDX) spectrum (Figure S1d, Supporting Information) confirm the successful synthesis of monodispersed hexagonal CdS QDs with an average size of $\approx 10\text{--}20 \text{ nm}$. The HAADF-STEM image and corresponding elemental mapping images (Figure S2, Supporting Information) also corroborate the successful fabrication of CdS QDs.^[24,25] In comparison, the TEM and HAADF-STEM images of Ru0.1 (Figure S3a,b, Supporting Information) show the monodispersed Ru0.1 with similar sizes, suggesting no difference in the morphology/size distribution between Ru0 and Ru0.1. Figure 1a indicates the lattice spacing values of 3.6 and 3.6 \AA with an angle of 120.0° , corresponding to the (010) and (-100) facets of hexagonal CdS, respectively. Atomic-Resolution HAADF-STEM image combined with EDX elemental mapping of Ru signal (Figure 1b) confirms the incorporation of Ru atoms in CdS QDs in Ru0.1. As shown in Figure 1b, isolated Ru atom is observed in the three selected regions (i.e., 1, 2, and 3) of Ru0.1, as confirmed by the corresponding line analyses of EDX Ru signals (Figure 1c–e). Given the very close atomic number of Ru ($Z = 44$) and Cd ($Z = 48$), the existence of Ru atoms is revealed via the EDX signal as shown by the red peaks in Figure 1c–e. Thus, the accurate Ru atom sites along the line in regions 1–3 are revealed by the red peak positions. The blue peaks in Figure 1c–e correspond to the HAADF-STEM contrast signal. As shown in Figure 1c–e, the blue peaks show almost the same intensities at the Ru sites location, compared to the other peaks at locations without Ru. These results imply that Ru is incorporated into the crystal structure of Ru0.1 via replacing the Cd sites, rather than loading on the surface of CdS QDs.^[26] No Ru_xS_y /Ru clusters or nanoparticles can be observed in the HAADF-STEM images of Ru0.1 (Figure 1a,b; Figure S3b, Supporting Information), also corroborating the successful incorporation of Ru atoms in CdS QDs via the in situ hot-injection route. Besides, additional results of Ru0.1 in Figure S4 (Supporting Information) also imply that Ru atom is incorporated into the crystal structure of CdS QDs via replacing the Cd site. Moreover, the HAADF-STEM image (Figure 1f) and corresponding elemental mapping images (Figure 1g–i) of Ru0.1 also further indicate the homogeneous distribution of Ru atoms onto CdS QDs. Furthermore, the successful incorporation of Ru atoms in CdS QDs for Ru0.1 is confirmed by the inductively coupled plasma-atomic emission spectroscopy (ICP-AES), revealing the very low content of Ru (0.07 wt%) in Ru0.1. This value is only slightly lower than the nominal weight ratio (0.1 wt%) for Ru0.1. The X-ray diffraction (XRD) patterns of all the as-synthesized samples (Figure S5, Supporting Information) indicate the existence of hexagonal wurtzite-structured CdS only (JCPDS #77-2306). No other peaks are found in the XRD patterns of Ru0.05, Ru0.1, and Ru0.2, suggesting no Ru_xS_y or Ru nanoparticles/clusters exist in these samples.^[27]

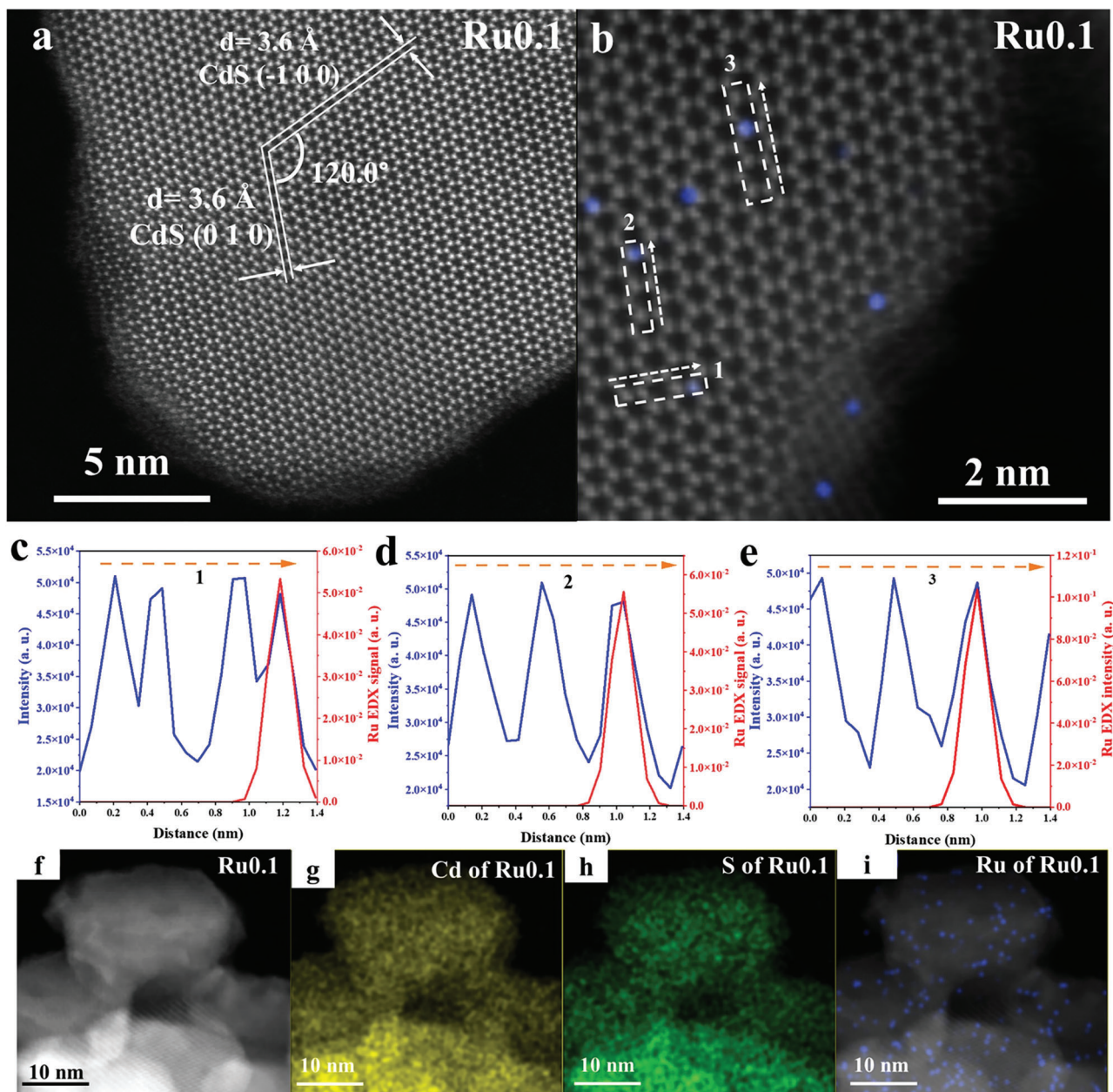


Figure 1. a) Atomic-Resolution HAADF-STEM image of Ru0.1. b) Atomic-Resolution HAADF-STEM image combined with EDX elemental mapping of Ru signals for Ru0.1, and corresponding line analyses of HAADF-STEM contrast signals combined with EDX Ru signals in regions c) 1, d) 2, and e) 3. f) HAADF-STEM image and corresponding elemental mapping images of g) Cd, h) S, and i) Ru for Ru0.1.

This also supports the incorporation of Ru atoms into CdS QDs for Ru0.1. CdS phases in Ru0 and Ru0.1 are also confirmed by the strong first-order longitudinal optical (1LO) phonon and the relatively weak second-order longitudinal optical (2LO) phonon modes in the Raman spectra (Figure S6, Supporting Information).^[28]

The intense electronic interaction between incorporated Ru and CdS QDs in Ru0.1 is revealed by both high-Resolution X-Ray photoelectron spectroscopy (XPS) and synchrotron-based X-Ray absorption near edge structure (XANES). No obvious shift of Cd 3d peaks is found for Ru0.1 compared to those of Ru0

(Figure S7a, Supporting Information). This is because the incorporated Ru replaces the Cd sites and connects to S atoms only, thus imposing negligible influence on the chemical states of Cd atoms. In comparison, the S 2p peaks of Ru0.1 are moved to the higher binding energy direction in comparison to those of Ru0, implying the electron transfer from S to Ru after Ru atoms are incorporated into CdS QD via replacing the Cd site.^[29,30] This is ascribed to the strong electron-extracting capacity of incorporated Ru³⁺ with a higher oxidation state (+3) than that of Cd²⁺ replaced. Unfortunately, due to the very low content of Ru (0.07 wt%) in Ru0.1 revealed by ICP-AES, the XPS signals of Ru cannot be

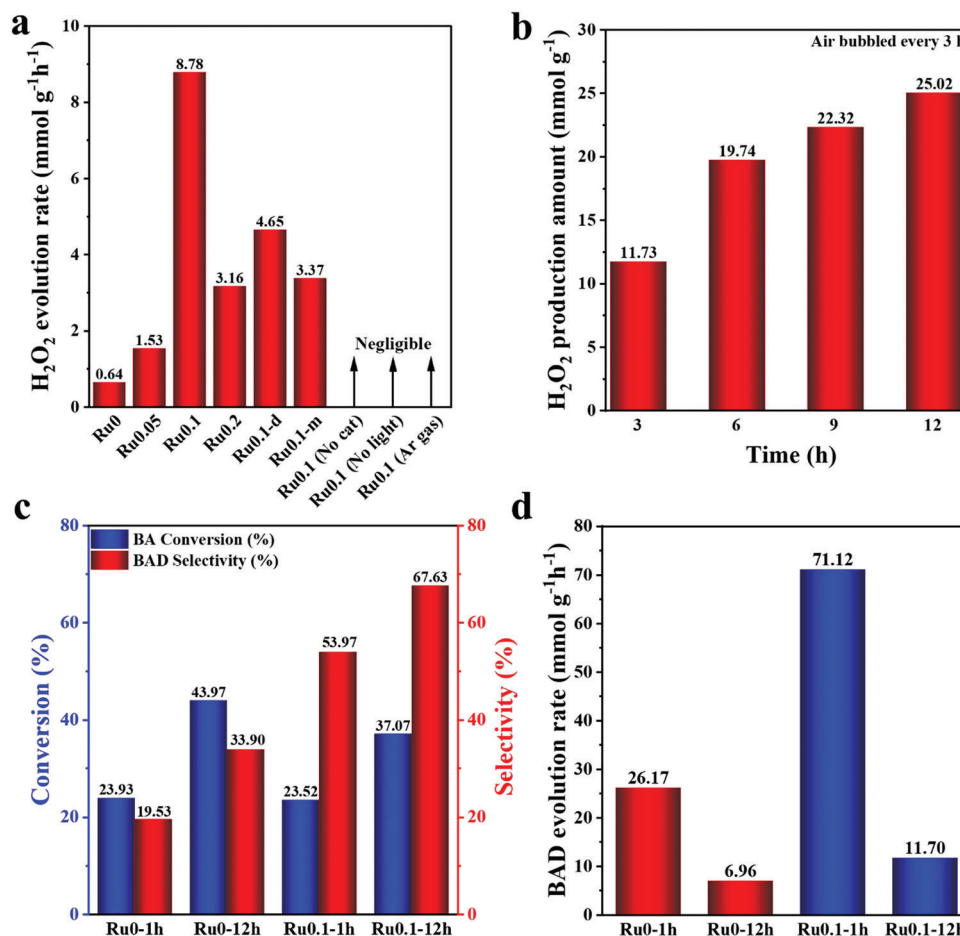


Figure 2. a) Photocatalytic H₂O₂ evolution rates of Ru0, Ru0.05, Ru0.1, Ru0.2, Ru0.1-d, and Ru0.1-m in BA aqueous solution using 420 nm LED light. The blank experiment results are also shown in Figure 2a. b) -hour stability test of photocatalytic H₂O₂ evolution on Ru0.1 in BA aqueous solution using 420 nm LED light. c) BA conversion and BAD selectivity for Ru0 and Ru0.1 in BA aqueous solution using 420 nm LED light. d) First-hour BAD evolution rates and 12 h averaged BAD evolution rates using Ru0 or Ru0.1 in BA aqueous solution using 420 nm LED light.

detected, since its content is below the detection limit of XPS technique. Synchrotron-based XANES spectra of S *K*-edge (Figure S8, Supporting Information) exhibit the obvious movement of S *K*-edge for Ru0.1 toward higher photon energy direction, also indicating the transfer of electron from S to Ru after incorporation of Ru atoms in CdS QDs. Therefore, based on the above HAADF-STEM, EDX spectra, EDX elemental mapping, XPS, and synchrotron-based XANES results, it is confirmed that Ru atoms are successfully incorporated into the crystal structure of CdS QDs in Ru0.1 via replacing the Cd sites.

To further highlight the key role of incorporated Ru atoms in Ru0.1 synthesized by the in situ hot-injection route, we have also fabricated 0.1 wt% Ru NPs loaded CdS QDs (Ru0.1-m) by mechanically mixing the as-synthesized Ru NPs with CdS QDs and 0.1 wt% Ru clusters/nanoparticles (NPs) loaded CdS QDs (Ru0.1-d) via photo-deposition, respectively. All the synthesis details are explained in the Supporting Information. Figure S9 (Supporting Information) shows no obvious difference in the XRD patterns of Ru0.1-m or Ru0.1-d compared to that of Ru0.1, due to the very low content of Ru clusters and/or nanoparticles on them. The TEM, HRTEM and EDX elemental mapping images of Ru0.1-m

and Ru0.1-d (Figures S10 and S11, Supporting Information) also confirm the successful loading of Ru clusters/NPs on CdS QDs.

2.2. Excellent Performances for H₂O₂ and Benzaldehyde Generation

Photocatalytic simultaneous generation of H₂O₂ and benzaldehyde (BAD) on all the samples were studied in benzyl alcohol (BA) aqueous solution in the air using a 420 nm light emitting diode (LED). UV-vis absorption spectra and corresponding standard curve of H₂O₂ aqueous solutions at different concentrations are shown in Figure S12a,b (Supporting Information), respectively. The H₂O₂ evolution rates in this work were calculated based on the standard curve and corresponding fitting parameters (Figure S12b, Supporting Information). Ru0 only exhibits a photocatalytic H₂O₂ evolution rate of 0.64 mmol g⁻¹ h⁻¹ (Figure 2a) owing to the rapid recombination of photo-induced electron-hole pairs and insufficient active sites on the surface. The in situ incorporation of Ru atoms in CdS QDs leads to obvious raise in H₂O₂ evolution for Ru0.05, Ru0.1, and Ru0.2

(Figure 2a). Especially, Ru0.1 exhibits the highest H_2O_2 evolution rate of $8.78 \text{ mmol g}^{-1} \text{ h}^{-1}$, $\approx 1372\%$ times larger than that of Ru0. To the best of our knowledge, this rate is one of the highest among the reported photocatalysts (Figure S13 and Table S1, Supporting Information). Notably, compared to Ru0.1, an obvious reduction in the activity is observed for Ru0.2, possibly due to the excessive Ru loading blocking light absorption and covering surface active sites.^[31] To confirm that the generated H_2O_2 arises from photocatalytic O_2 reduction, blank experiments were conducted without photocatalyst or without light illumination or in Argon atmosphere, while all the other experimental conditions remain the same. No H_2O_2 evolution was observed for Ru0.1 in all the above blank experiments (Figure 2a), suggesting that H_2O_2 was generated via photocatalytic O_2 reduction of Ru0.1 with light illumination. To highlight the superiority of Ru-atoms incorporation, the H_2O_2 evolution rates were also tested on Ru0.1-m and Ru0.1-d, respectively. Obviously lower H_2O_2 evolution activities are observed for Ru0.1-d ($4.65 \text{ mmol g}^{-1} \text{ h}^{-1}$) or Ru0.1-m ($3.37 \text{ mmol g}^{-1} \text{ h}^{-1}$), compared to that of Ru0.1 ($8.78 \text{ mmol g}^{-1} \text{ h}^{-1}$). These results confirm the superior role of incorporated Ru atoms in CdS QDs compared to loaded Ru clusters/NPs on CdS QDs for raising photocatalytic H_2O_2 evolution.^[31] Additionally, Ru0.1 shows an apparent quantum efficiency (AQE) of 8.3% at 420 nm for H_2O_2 evolution. The H_2O_2 evolution rates of Ru0 and Ru0.1 with xenon light illumination ($\lambda > 400 \text{ nm}$) were studied and the results are shown in Figure S14 (Supporting Information). Ru0.1 exhibits $\approx 258\%$ times higher H_2O_2 evolution rate ($3.82 \text{ mmol g}^{-1} \text{ h}^{-1}$) compared to that of Ru0 ($1.48 \text{ mmol g}^{-1} \text{ h}^{-1}$). Furthermore, the stability of photocatalytic H_2O_2 evolution for Ru0.1 was tested for 12 h, while the other reaction conditions remain the same. The accumulative H_2O_2 evolution amounts were acquired every 3 h. As shown in Figure 2b, accumulative H_2O_2 generation exhibits an obvious surge from 11.73, 19.74, 22.32 to 25.02 mmol g^{-1} throughout the 12 h test (Figure 2b). Nevertheless, Figure S15 (Supporting Information) shows a downward trend for H_2O_2 evolution from 11.73 mmol g^{-1} (0–3 h) to 8.01 mmol g^{-1} (4–6 h), 2.58 mmol g^{-1} (7–9 h), and 2.70 mmol g^{-1} (10–12 h), respectively. The reasons for this obvious reduction in H_2O_2 evolution of Ru0.1 are summarized as follows: i) the generated H_2O_2 is susceptible to decomposition ($\text{H}_2\text{O}_2 + \text{H}^+ + \text{e}^- \rightarrow \text{H}_2\text{O} + \cdot\text{OH}$; $\text{H}_2\text{O}_2 \rightarrow 2\cdot\text{OH}$), which becomes more severe as H_2O_2 concentration increases; ii) as the concentration of hole scavenger (BA) decreases, the available photo-induced electrons in Ru0.1 would decline, also leading to the reduced H_2O_2 evolution.^[19,32] For the photocatalytic oxidation reactions of Ru0.1, the conversion of BA and selectivity of BAD are also acquired. As displayed in Figure 2c, Ru0 exhibits a BA conversion of 23.93% and a BAD selectivity of 19.53% in the first hour, as well as a BA conversion of 43.97% and a BAD selectivity of 33.90% in the 12 h reaction. In comparison, Ru0.1 shows a BA conversion of 23.52% and a BAD selectivity of 53.97% in the first hour, together with a BA conversion of 37.07% and a BAD selectivity of 67.63% in the 12 h reaction. Furthermore, it is interesting to observe that compared with Ru0, Ru0.1 exhibits almost the same first-hour BA conversion (23.52%) and even lower 12 h BA conversion (37.07%). Nevertheless, we also find that compared to Ru0, Ru0.1 shows both much higher first-hour BAD selectivity (53.97%) and 12 h BAD selectivity (67.63%). These findings reveal that the incorporated Ru atoms in CdS QDs im-

pose no or even negative effects on the BA conversion. However, the incorporated Ru atoms can obviously raise the BAD selectivity.

Based on the results in Figure 2c, we have calculated the first-hour and 12 h averaged BAD evolution rates of both Ru0 and Ru0.1 as shown in Figure 2d. Compared to Ru0 (26.17 and $6.96 \text{ mmol g}^{-1} \text{ h}^{-1}$), Ru0.1 exhibits the much higher first-hour ($71.12 \text{ mmol g}^{-1} \text{ h}^{-1}$), and 12 h averaged ($11.70 \text{ mmol g}^{-1} \text{ h}^{-1}$) evolution rates for BAD evolution. These results disclose that the incorporated Ru atoms in CdS QDs (Ru0.1) can obviously raise the BAD selectivity, thus leading to the enhancement of BAD evolution rates in photocatalytic reactions.

To study the stability of Ru0.1 after the 12 h reaction (annotated as Ru0.1-R), XRD, Raman, TEM, EDX analysis, and atomic-Resolution HAADF-STEM were adopted. The corresponding results (Figures S16–S18, Supporting Information) confirm that no obvious change of the crystal structure, morphology, size distribution, and atomic-level compositions/structures for Ru0.1-R is observed, compared to those of Ru0.1. These results strongly corroborate the Robustness of Ru0.1 on photocatalytic H_2O_2 and BAD generation.

2.3. Light Absorption and Band Structures

To investigate the reason for the excellent performances of Ru0.1, the light absorption, charge separation/transfer, and surface redox reactions of Ru0.1 were studied by a range of advanced characterizations, such as quasi in situ X-Ray photoelectron spectroscopy (XPS), in situ atomic force microscopy (AFM)-Kelvin probe force microscopy (KPFM), in situ transient-state surface photovoltage (SPV) spectroscopy, in situ ultrafast transient absorption spectroscopy (TAS), and in situ diffuse reflectance infrared Fourier transform spectroscopy (DRIFTS). First, the light absorption abilities of all the samples are studied by UV-vis diffuse reflectance spectroscopy. The UV-vis diffuse reflectance spectra (Figure S19, Supporting Information) show the gradually red-shifted absorption edge in the order of Ru0, Ru0.05, Ru0.1, and Ru0.2, corresponding to the increasingly-narrowed bandgaps of 2.17, 2.06, 2.04, and 2.00 eV, respectively.^[33] This is ascribed to the incorporation of Ru atoms into the crystal structure of CdS QDs, resulting in narrowed bandgaps.

To study the effect of light wavelengths on the photocatalytic performances of Ru0.1, we have tested the photocatalytic H_2O_2 evolution of Ru0.1 using LED lights with different wavelengths of 365, 420, 550, and 740 nm, respectively. As shown in Figure S20 (Supporting Information), Ru0.1 exhibits the H_2O_2 evolution rates of 9.47, 8.78, and $1.78 \text{ mmol g}^{-1} \text{ h}^{-1}$ using the LED lights with wavelengths at 365, 420, and 550 nm, respectively. Additionally, negligible H_2O_2 evolution is observed on Ru0.1 with 740 nm LED illumination (Figure S20, Supporting Information), suggesting that the raised light absorption in the range of ≈ 600 –800 nm possibly doesn't contribute to the H_2O_2 evolution for Ru0.1.

To study the electronic band structures of Ru0 and Ru0.1, the Mott–Schottky (M–S) plots, and XPS valence band (VB) spectra were collected.^[34] Figure S21 (Supporting Information)

exhibits that the flat band potentials of Ru0 and Ru0.1 are -0.65 and -0.61 V versus Ag/AgCl electrode, corresponding to -0.05 and -0.01 versus the reversible hydrogen electrode (RHE), respectively. Besides, Ru0 and Ru0.1 exhibit the VB edge positions at 1.56 and 1.38 V versus their Fermi levels, respectively (Figure S22, Supporting Information). Thus, the VB edge positions of Ru0 and Ru0.1 are determined to be 1.51 and 1.37 V versus RHE. And the conduction band (CB) edge positions of Ru0 and Ru0.1 are calculated to be -0.66 and -0.67 V versus RHE. Accordingly, their electronic band structures are depicted in Figure S23 (Supporting Information). As displayed in Figure S23 (Supporting Information), the reduction ability of photo-generated electrons on the CB of Ru0.1 is almost the same as that of Ru0, but the oxidation capacity of photo-generated holes on the VB of Ru0.1 is slightly weaker than that of Ru0. This weaker oxidation ability of Ru0.1 than that of Ru0 could possibly lead to the lower BA conversion Ru0.1, compared with that of Ru0 (Figure 2d). Nevertheless, the light responsive range of Ru0.1 is extended compared to that of Ru0.

2.4. Photo-Generated Electrons/Holes Separation/Transfer Mechanism

Then, the photo-generated electrons/holes separation/transfer mechanism in Ru0.1 was studied by four different kinds of (quasi) in situ characterizations, including quasi in situ XPS, in situ AFM-KPFM, in situ transient-state SPV spectroscopy, and in situ ultrafast TAS. We adopt these four in situ characterizations since they can provide element/space/time-resolved information about the distribution/separation/transfer/recombination of photo-generated electrons and holes, respectively, in or on the surface of photocatalysts at different conditions, such as with light illumination and certain electron/hole scavengers. First, surface-sensitive quasi in situ XPS technique was utilized to provide the steady-state element-resolved information about the photo-generated electrons/holes distribution on/near the surface of Ru0 and Ru0.1 in a vacuum environment. As shown in Figure 3a,b, with light illumination, both Cd $3d$ and S $2p$ peaks of Ru0 exhibit the right shift to higher binding energy direction, compared to those of Ru0 without light. These results indicate the accumulation of more photo-generated holes than electrons on/near the surface of CdS QDs with light on and in vacuum environment.^[25] This is attributed to the upward bending of CB and VB for Ru0 (CdS) as an *n*-type semiconductor, which to some extent drives the photo-generated holes to the surface and impedes the photo-generated electrons transferring to the surface. Interestingly, this trend is reversed for Ru0.1 in the same conditions. As displayed in Figure 3c,d, with light on, the Cd $3d$ and S $2p$ peaks of Ru0.1 shift to the lower binding energy direction, in contrast with those of Ru0.1 with light off. These results are attributed to the incorporation of Ru atoms in Ru0.1. The high oxidation state (+3) of Ru leads to the directional flow of photo-generated electrons from the bulk to the surface of Ru0.1, thus resulting in the accumulation of more photo-generated electrons than holes on the overall surface of Ru0.1. It should be noted that Ru atoms not only attract the photo-generated electrons around themselves, but, more importantly, raise the dis-

tribution of photo-generated electrons on the overall surface (Cd and S elements) of Ru0.1, as revealed by the element-resolved results in Figure 3c,d.^[35] Furthermore, these quasi in situ XPS results (Figure 3) are acquired in the vacuum environment, in which there is no interference by the electron scavenger (e.g., O_2 in the air) and/or hole scavenger (e.g., sacrificial electron donor). Thus, these results are only determined by the intrinsic physico-chemical properties of Ru0 and Ru0.1. Furthermore, in situ AFM-KPFM technique was applied to reveal the steady-state space-resolved information about the distribution of photo-generated electrons/holes on the surface of Ru0.1 with light illumination and in air. The AFM image and corresponding height profile for the large aggregation of Ru-incorporated CdS QDs (Ru0.1) are shown in Figure S24 (Supporting Information). This aggregation in Ru0.1 is due to the high surface energy of Ru-incorporated CdS QDs with a very small average size of ≈ 10 – 20 nm, as shown in the TEM image of Ru0.1 (Figure S3a, Supporting Information). The KPFM image of the same region in Ru0.1 (Figure 4a) shows the corresponding surface potential map of Ru0.1 in darkness. The corresponding potential profile along the line scan between points 1 and 1' is displayed in Figure 4b. The potential difference between the highest potential point of Ru0.1 and the base is ≈ 40 mV in darkness. In contrast, Figure 4c exhibits the KPFM image of the same region in Ru0.1 with light illumination. Figure 4d shows the corresponding potential profile along the same line scan between points 2 and 2'. With light on, the potential difference between the highest potential point and the base is raised to ≈ 50 mV. Raise on the potential difference along the same line scan (Figure 4b,d) for Ru0.1 indicates the accumulation of more photo-generated holes than electrons on the overall surface of Ru incorporated CdS QDs in Ru0.1 with light on and in air.^[36] Interestingly, this result seems contradictory to the trend shown by the quasi in situ XPS results of Ru0.1 (Figure 3c,d) with light on and in vacuum environment. Actually, the reason is that in air environment the strong electron scavenger, O_2 , adsorbed on the surface of Ru0.1 can efficiently capture the majority of photo-generated electrons accumulated on Ru0.1, leaving much more photo-generated holes than electrons on the surface of Ru0.1.

Then, we further employed two different transient-state in situ characterizations (i.e., transient-state SPV and TAS) to provide the time-resolved information about the dissociation/transfer/recombination of photo-generated electrons/holes in Ru0.1 at different conditions. First, in situ transient-state SPV was utilized to explore the kinetics for photo-generated electrons/holes in a time scale of ≈ 0.07 μ s to 1 ms after light excitation on the surface of Ru0 and Ru0.1 in air. As shown in Figure 5a, Ru0 exhibits the positive SPV signal in the whole range of ≈ 0.07 μ s to 1 ms. The highest positive SPV signal (≈ 0.0025 mV) is achieved by Ru0 at ≈ 0.14 μ s, followed by the gradual decay of positive SPV signal to zero at ≈ 0.29 ms. This result is also in accordance with the above steady-state quasi in situ XPS results (Figure 3a,b) for Ru0. In comparison, Ru0.1 first exhibits the negative SPV signal in the range of ≈ 0.079 to ≈ 0.11 μ s and then shows the positive SPV signal, which reaches the highest value of ≈ 0.025 mV at ≈ 0.115 μ s. Subsequently, Ru0.1 exhibits the gradual decay of positive SPV signal, which reaches zero at ≈ 0.2 ms. The reason is that the incorporated Ru atoms in CdS QDs first efficiently attract the transfer of photo-generated electrons from

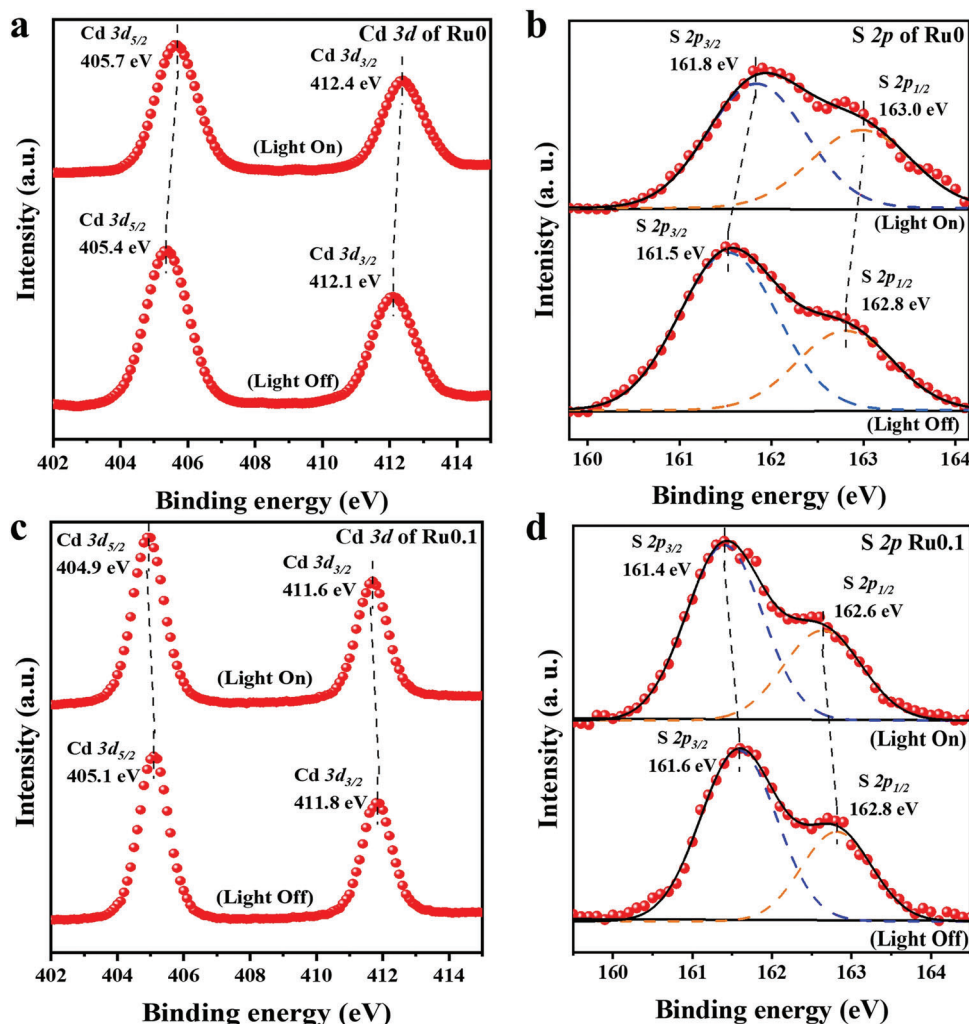


Figure 3. High-Resolution XPS spectra of a) Cd 3d and b) S 2p for Ru0 with light on and off, respectively. High-Resolution XPS spectra of c) Cd 3d and d) S 2p for Ru0.1 with light on and off, respectively.

the bulk to the surface, leading to more photo-generated electrons than holes on the surface of Ru0.1.^[37] Thus, Ru0.1 first exhibits the negative SPV signal before $\approx 0.11 \mu\text{s}$. Nevertheless, the strong electron scavenger, O_2 , adsorbed on the surface of Ru0.1 rapidly captures these photo-generated electrons, resulting in more photo-generated holes than electrons remaining on the surface of Ru0.1. Hence, Ru0.1 starts to show the positive SPV signal after $\approx 0.11 \mu\text{s}$. Eventually, these photo-generated holes recombine with the photo-generated electrons on the surface of Ru0.1, finally leading to the decay of SPV signal to zero at $\approx 0.2 \text{ ms}$ (Figure 5a). Notably, Ru0.1 shows the highest SPV signal of $\approx 0.025 \text{ mV}$, ≈ 10 times larger than that of Ru0 (Figure 5a). The reason is that the incorporated Ru atoms in Ru0.1 can effectively trap the electrons to avoid their recombination with the photo-generated holes, thus resulting in more holes transferred to the surface compared to those of Ru0.^[38,39] Besides, the highest SPV signal of Ru0.1 is achieved at $\approx 0.115 \mu\text{s}$, faster than that of Ru0 attained at $\approx 0.14 \mu\text{s}$, suggesting the faster migration of photo-generated holes in Ru0.1 than those in Ru0. Furthermore,

in situ ultrafast TAS was utilized to study the kinetics of photo-generated electrons/holes in a time scale of 0 to $\approx 3100 \text{ ps}$ for both Ru0 and Ru0.1 dispersed in ethanol solution and in air, in which the ethanol and dissolved O_2 serve as the hole and electron scavenger, respectively. As shown in Figure 5b,c, both Ru0 and Ru0.1 show the positive and negative absorption bands, ascribed to the excited-state absorption (ESA) and ground-state bleaching (GSB) signals, respectively. Actually, ESA signals arise from the photo-excited electrons in the CB of Ru0 and Ru0.1; GSB signals are directly related to the photo-excited holes in the VB of Ru0 and Ru0.1. Hence, the decay kinetics of ESA and GSB signals can be regarded as the decay kinetics of photo-excited electrons and holes, respectively. Furthermore, Figure S25a,b (Supporting Information) exhibits the ultrafast TA spectra of Ru0 and Ru0.1 at different pump-probe delay times, respectively. As displayed in Figure S25a,b (Supporting Information), the GSB peaks of Ru0 and Ru0.1 exhibit some redshifts to the longer wavelength direction. This is attributed to the size variations of CdS QDs (Ru0) and Ru-incorporated CdS QDs (Ru0.1), in which smaller-sized CdS

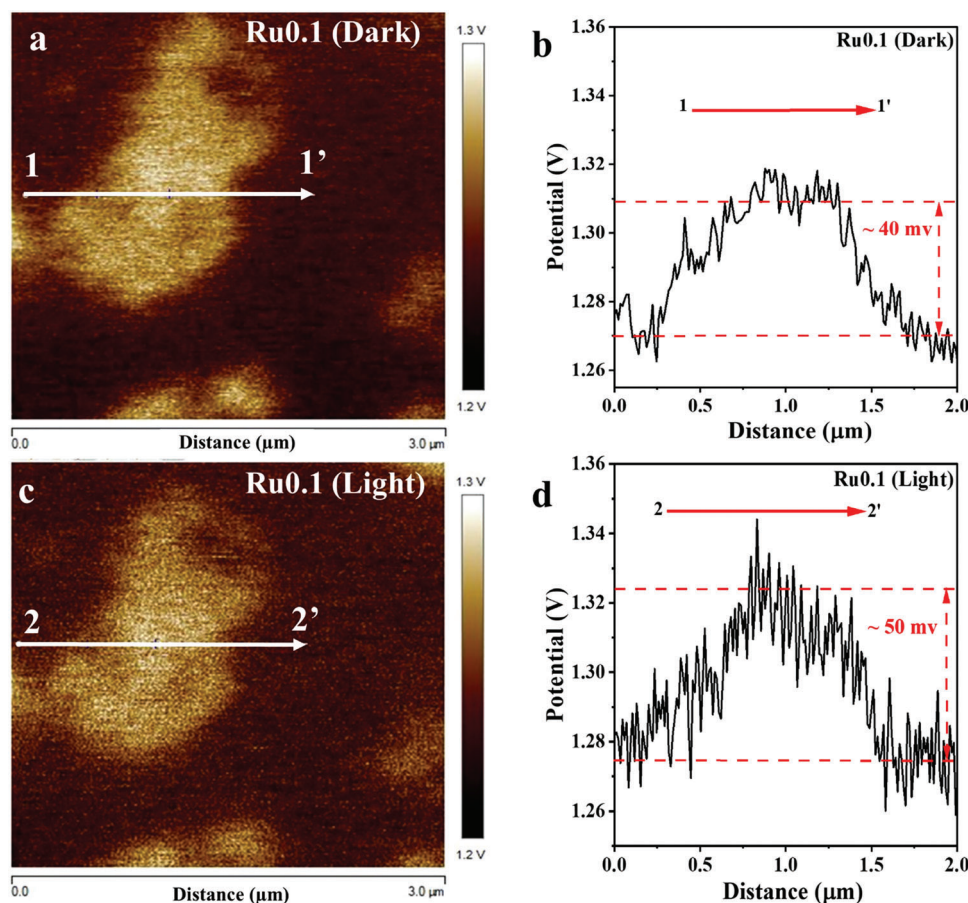


Figure 4. a) In situ KPFM image and b) corresponding potential profile along 1 to 1' line of Ru0.1 in darkness. c) In situ KPFM image and d) corresponding potential profile along 2 to 2' line of Ru0.1 with light illumination.

or Ru-incorporated CdS QDs possess the bigger bandgaps and more rapid exciton annihilation. Furthermore, to simulate the realistic reaction conditions of Ru0 and Ru0.1 for photocatalytic H_2O_2 and BAD generation, we use dissolved O_2 and ethanol as the electron and hole scavengers, respectively, for both Ru0 and Ru0.1. In these conditions, we investigate the decay kinetics of photo-excited electrons and holes by studying the decay kinetics of ESA and GSB signals, respectively. As shown in Figure 5d, the ESA signals of Ru0.1 decay obviously slower than those of Ru0, suggesting that the incorporated Ru in CdS QDs can apparently raise the lifetimes of photo-generated electrons, in the existence of both electron and hole scavengers. This is ascribed to the strong electron-extracting ability of Ru with high oxidation state (+3). Moreover, Ru0.1 also exhibits the slower decay kinetics of GSB signals, compared to Ru0 (Figure 5e). Nevertheless, the decay kinetics difference of GSB signals between Ru0 and Ru0.1 is obviously smaller than the decay kinetics difference of ESA signals between Ru0 and Ru0.1. The reason is that the incorporated Ru atoms in Ru0.1 only impose the indirect effect on the photo-excited holes via trapping photo-excited electrons to impede their recombination with holes.^[36,40] Based on the ESA/GSB signal intensities for the fitting Results of Ru0/Ru0.1 at ≈ 3100 ps (Figure 5d,e), we can estimate that Ru0 reserves $\approx 8\%$ photo-excited electrons and $\approx 18\%$ photo-excited holes at

≈ 3100 ps; Ru0.1 retains $\approx 16\%$ photo-excited electrons and $\approx 20\%$ photo-excited holes at ≈ 3100 ps. Furthermore, the faster decays of ESA signals than GSB signals are observed for both Ru0 and Ru0.1 in the time range of 0– ≈ 3100 ps (Figure S25c,d, Supporting Information), attributed to dissolved O_2 as a strong electron scavenger, compared to ethanol as a moderate hole scavenger. Notably, in situ transient-state SPV provides the charge kinetics information in the time scale of 70 ns–1 ms; whilst in situ TAS supplies the charge dynamics information in the time scale of 0–3.1 ns. It is challenging to accurately correlate the information acquired from the above two in situ techniques, since the excitation light wavelength/intensity, test environments (solid-state catalyst in air or catalyst suspended in ethanol) and test information (SPV on the surface of catalyst or transient absorption of the whole catalyst) are different. Thus, we successfully utilized four different (quasi) in situ characterizations to provide the element/space/time-resolved information on the kinetics of photo-generated electrons and holes in Ru0.1. All the results and conclusions are summarized in Table S3 (Supporting Information).

Finally, we utilize the transient-state photoluminescence (PL) spectroscopy and transient photocurrent (TPC) measurement to study the overall separation/transfer/recombination efficiency of photo-generated electrons and holes in Ru0.1. Figure S26

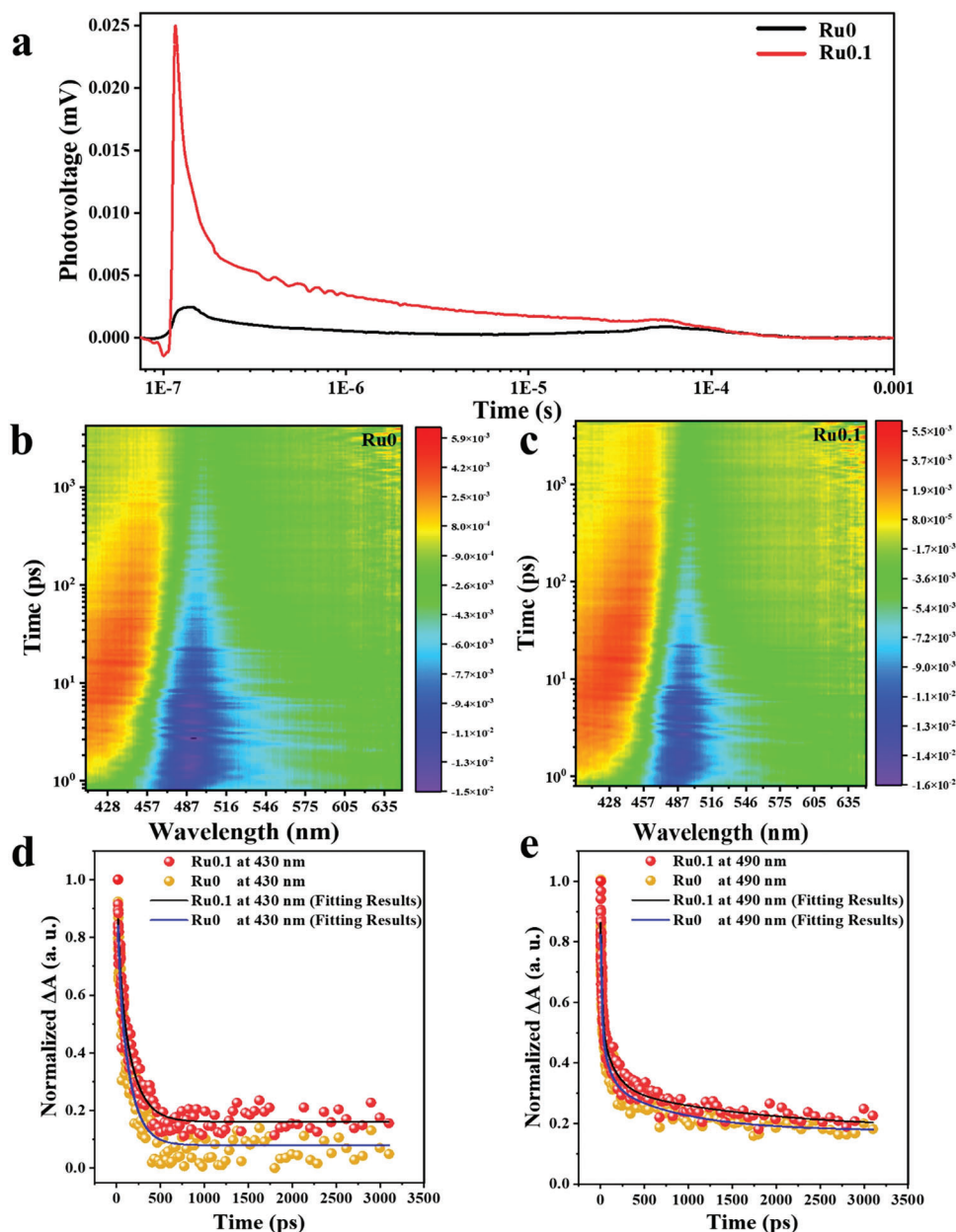


Figure 5. a) In situ transient-state SPV spectra of Ru0 and Ru0.1. 2D pseudo-color in situ TA spectra of b) Ru0 and c) Ru0.1 in ethanol solution after the excitation with a 400 nm laser pulse. d) Normalized decay kinetics and fitting lines for Ru0 and Ru0.1 were taken through the ESA peaks at 430 nm, respectively. e) Normalized decay kinetics and fitting lines for Ru0 and Ru0.1 taken through the GSB peaks at 490 nm, respectively.

(Supporting Information) shows the transient-state PL decay spectra of Ru0 and Ru0.1. The slower decay of PL spectrum and the longer averaged charge lifetime ($\tau_{\text{ave}} = 0.72$ ns) of Ru0.1 compared to that of Ru0 ($\tau_{\text{ave}} = 0.31$ ns) indicate the inhibited charge recombination in Ru0.1 after incorporating Ru atoms.^[41] Furthermore, the TPC density measurement results (Figure S27, Supporting Information) indicate the much higher current density of Ru0.1 compared to that of Ru0, again confirming the much more efficient separation/migration of photo-excited electrons/holes after incorporation of Ru atoms into CdS QDs in Ru0.1.^[42]

2.5. Redox Reaction Mechanisms

The surface redox reaction mechanisms for the photocatalytic generation of H₂O₂ and BAD were studied using in situ DRIFTS, electron spin resonance (ESR) spectroscopy, species-trapping experiment, and electron transfer number/H₂O₂ selectivity test. To deeply investigate the surface reaction process over Ru0.1 for photocatalytic reduction of O₂ to form H₂O₂ and oxidation of BA to generate BAD, the in situ DRIFTS spectroscopy was adopted. First, Ru0.1 was bubbled with O₂ gas through the BA aqueous solution for 60 min to create the realistic reaction condition on

photocatalysis. Then, the light is turned on to drive the photocatalytic reaction. The DRIFTS spectra were collected consecutively before O₂/H₂O₂/BA bubbling, after 60 min O₂/H₂O₂/BA bubbling with 60 min light illumination and after the light was switched off. As illustrated in the DRIFTS spectra (Figure S28a,b, Supporting Information), only after both 60 min O₂/H₂O/BA bubbling and 60 min light illumination, two bands at 1208 and 1386 cm⁻¹ arise, assigned to the O—O stretching mode of surface-adsorbed superoxide ([•]OOH) and the OOH bending mode of surface-adsorbed hydroperoxide ([•]HOOH), respectively.^[43,44] These results reveal the generation of H₂O₂ on the surface of Ru0.1 via a superoxide intermediate pathway. Furthermore, after the light was switched off, these two bands at 1208 and 1386 cm⁻¹ become weaker, further corroborating the evolution of H₂O₂ via photocatalytic O₂ reduction on Ru0.1. Besides, we also observe two bands at 1715 and 2863 cm⁻¹, only after both 60 min O₂/H₂O/BA bubbling and 60 min light illumination. These two bands are ascribed to the stretching vibration of C=O bonds and stretching vibration of C—H bonds in aldehyde, respectively. With the light turned off, the intensities of these two bands are apparently reduced. These results confirm the generation of BAD via photocatalytic oxidation of BA. Furthermore, no obvious bands at 1208, 1386, 1715, and 2863 cm⁻¹ are observed before O₂/H₂O₂/BA bubbling or light illumination, again confirming that H₂O₂ and BAD are generated via photocatalytic O₂ reduction and BA oxidation of Ru0.1 with light illumination.

Then, ESR spectroscopy was adopted to detect the reactive oxygen species (ROS) in photocatalysis. In the blank experiments, no signals of DMPO·O₂⁻, TEMP·¹O₂, and DMPO·OH adducts were observed in darkness with Ru0.1 (Figure S29, Supporting Information).^[13] After 5 min light illumination, the characteristic signals of DMPO·O₂⁻ adduct can be observed, suggesting that the chemisorbed O₂ molecules on the surface of Ru0.1 were reduced by photo-excited electrons to form [•]O₂⁻. After 1 min light illumination, characteristic signals of TEMP·¹O₂ adduct can be found for Ru0.1, suggesting the generation of ¹O₂ ([•]O₂⁻ + h⁺ → ¹O₂). Additionally, characteristic signals of DMPO·OH are also observed for Ru0.1 after 5 min light illumination. Notably, the photo-induced holes on the VB of Ru0.1 cannot oxidize H₂O to form [•]OH, due to the more negative potential of VB edge position (1.37 V) compared to the potential of forming [•]OH (+2.4 V).^[45] Thus, the generation of [•]OH is deduced to arise from the decomposition of formed H₂O₂ (H₂O₂ + H⁺ + e⁻ → [•]OH + H₂O).

To further reveal the reaction mechanism, species quenching experiments were conducted. The corresponding results are displayed in Figure S30 (Supporting Information). The evolution rates of H₂O₂ are significantly reduced to 1.20 and 0.66 mmol g⁻¹ h⁻¹, respectively, as silver nitrate and ammonium oxalate were added into the system as scavengers of electrons (e⁻) and holes (h⁺), respectively. These results indicate the key roles of photo-induced e⁻ and h⁺ in the light-induced redox reactions. The addition of *p*-benzoquinone as the scavenger of [•]O₂⁻ significantly reduced the H₂O₂ evolution rate to negligible, indicating the decisive role of [•]O₂⁻ for photocatalytic H₂O₂ generation. Additionally, adding *L*-Tryptophan also dramatically decreases the H₂O₂ evolution rate to 1.12 mmol g⁻¹ h⁻¹. This result suggests that ¹O₂ is also involved in the H₂O₂ evolution reaction (¹O₂ + 2e⁻ + 2H⁺ → H₂O₂). Besides, another reason is that the consumption of ¹O₂ would result in the reduced amounts of both [•]O₂⁻

and h⁺ (O₂⁻ + h⁺ → ¹O₂), thus leading to the decreased H₂O₂ evolution rate. At last, the H₂O₂ evolution rate remains almost the same (≈8.8 mmol g⁻¹ h⁻¹) after adding isopropanol as the [•]OH scavenger. This result indicates that [•]OH is not involved in the generation of H₂O₂ for Ru0.1.^[13,46]

Moreover, the activity and selectivity of Ru0.1 for electrocatalytic H₂O₂ evolution via O₂ reduction reaction (ORR) were studied in O₂-saturated 0.1 M KOH solution by rotating ring-disk electrode (RRDE) tests. The H₂O₂ oxidation current (*J*_{Ring}) and O₂ reduction current (*J*_{disk}) were recorded on the ring and disk electrodes, respectively.^[44] Obvious reduction current below 0.4 V versus RHE is observed in Figure S31a (Supporting Information), suggesting the good catalytic efficiency of Ru0.1 for H₂O₂ evolution via two-electron ORR. Besides, the H₂O₂ evolution selectivity is reflected by the number of electrons transferred (*n*) in the actual reaction procedure, which was calculated to be 2.4 for Ru0.1 in the range of 0.30–0.55 V versus RHE. These results suggest the acceptable H₂O₂ evolution selectivity (≈53.36%–≈81.76%) in the range of 0.30–0.55 V versus RHE for Ru0.1 via the two-electron ORR (Figure S31b, Supporting Information).

Thus, based on the above results on ESR, species trapping and electrochemical tests, we raise the three possible reaction pathways for generating H₂O₂: i) [•]O₂⁻ + h⁺ → ¹O₂, ¹O₂ + 2e⁻ + 2H⁺ → H₂O₂; ii) O₂ + e⁻ → [•]O₂⁻, [•]O₂⁻ + e⁻ + 2H⁺ → H₂O₂; iii) O₂ + 2e⁻ + 2H⁺ → H₂O₂. Furthermore, the photocatalytic mechanism of Ru0.1 is displayed in Figure S32 (Supporting Information). With light illumination, the photo-induced electrons and holes are excited to the CB and VB of Ru0.1, respectively. Then, the photo-induced electrons transfer to the Ru atoms in Ru0.1, and photo-generated holes migrate to the surface of Ru0.1. Afterward, H₂O₂ can be formed via the three possible reaction pathways (Figure S32, Supporting Information). On the other hand, BA can be oxidized by the photo-generated holes or active oxygen species (e.g., [•]O₂⁻ and ¹O₂) to form various oxidation products, e.g., BAD. Notably, compared with active oxygen species with strongly oxidative abilities, the photo-generated holes with mild oxidative abilities tend to selectively oxidize BA into BAD.

Furthermore, for Ru0.1, the BAD evolution rate is obviously reduced from 71.12 mmol g⁻¹ h⁻¹ in the first hour to 11.70 mmol g⁻¹ h⁻¹ as the averaged rate in 12 h reaction (Figure 2d). The obvious reduction on BAD evolution rate is attributed to the following reasons: i) the generated BAD is further oxidized by photo-induced holes and/or active oxygen species (e.g., [•]O₂⁻) to form benzoic acid or other oxidation products, leading to decreased BAD evolution; ii) as the concentration of reactant (BA) decreases apparently, the evolution activity of product (BAD) also declines obviously.^[19] According to the results in Figure 2b,d, 0.1251 mol H₂O₂ and 0.702 mol BAD were generated by Ru0.1 in 12 h reaction. Theoretically, 0.2502 mol electrons and 1.404 mol holes were consumed to form H₂O₂ and BAD, respectively, suggesting that the photo-induced electrons and holes are not matched in the above redox reactions. Actually, some of the BAD was generated by the oxidation reaction between BA and the active oxygen species (e.g., [•]O₂⁻), which didn't consume photo-induced holes. And these active oxygen species were generated by the reaction between photo-induced electrons and O₂ in the air. Thus, the theoretically calculated electrons (0.2502 mol) and holes (1.404 mol) are not matched. Moreover, Ru0.1 shows the obviously raised

H₂O₂ evolution compared to Ru0 (Figure 2a). Besides, compared to Ru0, Ru0.1 exhibits similar or even lower BA conversions, but much higher BAD selectivity (Figure 2c). The possible mechanism is raised as follows: i) Ru atoms incorporated in Ru0.1 could raise the selectivity of two-electron ORR between photo-induced electrons and O₂ to directly form H₂O₂. Thus, the H₂O₂ evolution rate is obviously raised for Ru0.1, compared to that of Ru0; ii) since more electrons involve in the two-electron ORR for Ru0.1, less electrons involve in the reaction with O₂ to form active oxygen species, e.g., ·O₂·. Thus, less active oxygen species are generated and oxidize BA, leading to lower BA conversion of Ru0.1, compared with that of Ru0; iii) these active oxygen species with strongly oxidative abilities can oxidize BA to raise BA conversion, but could also over-oxidize BA to form benzoic acid or other oxidation products, leading to reduced BAD selectivity; iv) compared with the strongly oxidative active oxygen species, photo-induced holes in Ru0.1 possess relatively mild oxidation capacities to react with BA and form BAD selectively. Thus, compared to Ru0, Ru0.1 with Ru atoms exhibits the much higher H₂O₂ evolution rate and BAD selectivity, but much lower BA conversion.

3. Conclusion

Novel Ru-atom-incorporated monodispersed CdS quantum dots (QDs) were synthesized by an in situ hot injection route. The optimized sample (Ru0.1) exhibits the obviously-raised photocatalytic generation of H₂O₂ (8.78 mmol g⁻¹ h⁻¹) and benzaldehyde (BAD; 11.70 mmol g⁻¹ h⁻¹) using 420 nm light emitting diode (LED), compared with bare CdS QDs (Ru0). Four different in situ characterizations disclose that the incorporated Ru atoms with high oxidation state (+3) not only efficiently extract the photo-generated electrons from the bulk to the overall surface of Ru0.1, but also result in more photo-generated holes transferring onto the surface by retarding their recombination with electrons. In situ surface photovoltage (SPV) spectroscopy discloses that the strong electron scavenger, oxygen (O₂), could rapidly capture most of surface photo-excited electrons in ≈0.1 μs; the remaining photo-generated holes are up to ≈10 times more than those of Ru0. Besides, in situ TAS reveals that in realistic reaction conditions, Ru0.1 can reserve ≈16% photo-generated electrons at ≈3100 ps; whilst Ru0 can only retain ≈8% photo-generated electrons at the same time. Furthermore, the in situ diffuse reflectance infrared Fourier transform spectroscopy (DRIFTS) technique further confirms the generation of H₂O₂ and BAD with light illumination, O₂, water, and BA. The electron spin resonance (ESR) experiments combined with species quenching experiments further confirm the three different reaction pathways for H₂O₂ evolution. Our work demonstrates the importance of in situ characterizations providing the element/space/time-resolved information on electrons/holes kinetics and surface species generation in realistic conditions to instruct the atomic-level design/synthesis of high-activity photocatalysts toward desired reactions.

4. Experimental Section

Experimental details can be found in the Supporting Information.

Supporting Information

Supporting Information is available from the Wiley Online Library or from the author.

Acknowledgements

The authors gratefully acknowledge financial support from the Australian Research Council (ARC) through the Discovery Project Programs (FL170100154, DE200100629, and DP22102596) and Linkage Project (LP210301397 and CE230100032). The authors acknowledge the Australian Synchrotron (AS) for the XANES measurement at the soft X-Ray spectroscopy beamline. A.T.-K. acknowledges the support from the Australian Government Research Training Program Scholarship.

Open access publishing facilitated by The University of Adelaide, as part of the Wiley - The University of Adelaide agreement via the Council of Australian University Librarians.

Conflict of Interest

The authors declare no conflict of interest.

Data Availability Statement

The data that support the findings of this study are available from the corresponding author upon reasonable request.

Keywords

realistic charge kinetics, H₂O₂ evolution, in situ characterizations, Ru atoms

Received: May 25, 2023

Revised: July 19, 2023

Published online:

- [1] L. Zhang, R. Long, Y. Zhang, D. Duan, Y. Xiong, Y. Zhang, Y. Bi, *Angew. Chem., Int. Ed.* **2020**, 59, 6224.
- [2] Y. Chen, S. Ji, W. Sun, Y. Lei, Q. Wang, A. Li, W. Chen, G. Zhou, Z. Zhang, Y. Wang, L. Zheng, Q. Zhang, L. Gu, X. Han, D. Wang, Y. Li, *Angew. Chem., Int. Ed.* **2020**, 59, 1295.
- [3] C. Yang, W. W. Lee, H. Lin, Y. Dai, H. Chia, C. Chen, *RSC Adv.* **2016**, 6, 40664.
- [4] S. Li, L. Zhang, Y. Guo, Q. Zhang, M. Aleksandrak, E. Mijowskab, X. Chen, *New J. Chem.* **2022**, 46, 6319.
- [5] W. Zhang, C. Fu, J. Low, D. Duan, J. Ma, W. Jiang, Y. Chen, H. Liu, Z. Qi, R. Long, Y. Yao, X. Li, H. Zhang, Z. Liu, J. Yang, Z. Zou, Y. Xiong, *Nat. Commun.* **2022**, 13, 2806.
- [6] H. Zhuang, Z. Cai, W. Xu, M. Huang, X. Liu, *New J. Chem.* **2019**, 43, 17416.
- [7] T. Higashi, K. Seki, Y. Sasaki, Y. Pihosh, V. Nandal, M. Nakabayashi, N. Shibata, K. Domen, *Chem. - Eur. J.* **2023**, 29, e202204058.
- [8] L. Ma, M. Liu, D. Jing, L. Guo, *J. Mater. Chem. A* **2015**, 3, 5701.
- [9] C. Feng, Z. Wu, K. Huang, J. Ye, H. Zhang, *Adv. Mater.* **2022**, 34, 2200180.
- [10] Z. Fang, Y. Liu, C. Song, P. Tao, W. Shang, T. Deng, X. Zeng, J. Wu, *J. Semicond.* **2022**, 43, 041104.
- [11] P. Zhou, H. Chen, Y. Chao, Q. Zhang, W. Zhang, F. Lv, L. Gu, Q. Zhao, N. Wang, J. Wang, S. Guo, *Nat. Commun.* **2021**, 12, 4412.

- [12] X. Jiao, Z. Chen, X. Li, Y. Sun, S. Gao, W. Yan, C. Wang, Q. Zhang, Y. Lin, Y. Luo, Y. Xie, *J. Am. Chem. Soc.* **2017**, *139*, 7586.
- [13] J. Luo, X. Wei, Y. Qiao, C. Wu, L. Li, L. Chen, J. Shi, *Adv. Mater.* **2023**, *35*, 2210110.
- [14] X. Zhang, J. Yu, W. Macyk, S. Wageh, A. A. Al-Ghamdi, L. Wang, *Adv. Sustainable Syst.* **2023**, *7*, 2200113.
- [15] T. Shao, Y. Chang, Z. Li, Y. Song, D. Jin, J. Gao, L. Suncde, J. Hou, *J. Mater. Chem. A* **2023**, *11*, 1199.
- [16] Y. He, H. Rao, K. Song, J. Li, Y. Yu, Y. Lou, C. Li, Y. Han, Z. Shi, S. Feng, *Adv. Funct. Mater.* **2019**, *29*, 1905153.
- [17] Z. Teng, Q. Zhang, H. Yang, K. Kato, W. Yang, Y. Lu, S. Liu, C. Wang, A. Yamakata, C. Su, B. Liu, T. Ohno, *Nat. Catal.* **2021**, *4*, 374.
- [18] R. Y. Liu, M. Bae, S. L. Buchwald, *J. Am. Chem. Soc.* **2018**, *140*, 1627.
- [19] Y. Shiraishi, S. Kanazawa, D. Tsukamoto, A. Shiro, Y. Sugano, T. Hirai, *ACS Catal.* **2013**, *3*, 2222.
- [20] Z. Zheng, F. Han, B. Xing, X. Han, B. Li, *J. Colloid Interface Sci.* **2022**, *624*, 460.
- [21] W. Wang, W. Gao, X. Nie, W. Liu, X. Cheng, N. Shang, S. Gao, C. Wang, *J. Colloid Interface Sci.* **2022**, *616*, 1.
- [22] X. Chen, Y. Kuwahara, K. Mori, C. Louis, H. Yamashita, *ACS Appl. Energy Mater.* **2021**, *4*, 4823.
- [23] A. Behera, A. K. Kar, R. Srivastava, *Inorg. Chem.* **2022**, *61*, 12781.
- [24] X. Xiang, B. Zhu, B. Cheng, J. Yu, H. Lv, *Small* **2020**, *16*, 2001024.
- [25] J. Ran, H. Zhang, S. Fu, M. Jaroniec, J. Shan, B. Xia, Y. Qu, J. Qu, S. Chen, L. Song, J. M. Cairney, L. Jing, S.-Z. Qiao, *Nat. Commun.* **2022**, *13*, 4600.
- [26] Y. Zhang, J. Zhao, H. Wang, B. Xiao, W. Zhang, X. Zhao, T. Lv, M. Thangamuthu, J. Zhang, Y. Guo, J. Ma, L. Lin, J. Tang, R. Huang, Q. Liu, *Nat. Commun.* **2022**, *13*, 58.
- [27] Z. Zhang, M. Wang, H. Zhou, F. Wang, *J. Am. Chem. Soc.* **2021**, *143*, 6533.
- [28] T. Ahamad, M. A. Majeed Khan, S. Kumar, M. Ahamed, M. Shahabuddin, A. N. Alhazaa, *Appl. Phys. B* **2016**, *122*, 179.
- [29] S. Zhang, M. Du, Z. Xing, Z. Li, K. Pan, W. Zhou, *Appl. Catal., B* **2020**, *262*, 118202.
- [30] J. O. Olowoyo, M. Kumar, N. Singhal, S. L. Jain, J. O. Babalola, A. V. Vorontsov, U. Kumar, *Catal. Sci. Technol.* **2018**, *8*, 3686.
- [31] J. Wang, T. Xia, L. Wang, X. Zheng, Z. Qi, C. Gao, J. Zhu, Z. Li, H. Xu, Y. Xiong, *Angew. Chem., Int. Ed.* **2018**, *57*, 16447.
- [32] B. He, Z. Wang, P. Xiao, T. Chen, J. Yu, L. Zhang, *Adv. Mater.* **2022**, *34*, 2203225.
- [33] S. Liu, Y. Wang, S. Wang, M. You, S. Hong, T.-S. Wu, Y. L. Soo, Z. Zhao, G. Jiang, J. Qiu, B. Wang, Z. Sun, *ACS Sustainable Chem. Eng.* **2019**, *7*, 6813.
- [34] X. Wang, X. Wang, J. Huang, S. Li, A. Meng, Z. Li, *Nat. Commun.* **2021**, *12*, 4112.
- [35] S. Bai, H. Mei, W. Huang, M. Zhang, L. Cheng, *J. Materiomics* **2021**, *7*, 320.
- [36] P. Wang, S. Fan, X. Li, J. Wang, Z. Liu, Z. Niu, M. O. Tade, S. Liu, *Nano Energy* **2022**, *95*, 107045.
- [37] B. Mahrov, G. Boschloo, A. Hagfeldt, L. Dloczik, T. Dittrich, *Appl. Phys. Lett.* **2004**, *84*, 5455.
- [38] X. Wang, Y. Zhao, F. Li, L. Dou, Y. Li, J. Zhao, Y. Hao, *Sci. Rep.* **2016**, *6*, 24918.
- [39] L. Zhang, X. Zhu, Y. Zhao, P. Zhang, J. Chen, J. Jiang, T. Xie, *RSC Adv.* **2019**, *9*, 39604.
- [40] S. Zhang, H. Li, L. Wang, J. Liu, G. Liang, K. Davey, J. Ran, S. Qiao, *J. Am. Chem. Soc.* **2023**, *145*, 6410.
- [41] S. Wang, J. J. Zhang, M. Y. Zong, J. Xu, D. H. Wang, X. H. Bu, *ACS Catal.* **2022**, *12*, 7960.
- [42] L. Li, P. A. Salvador, G. S. Rohrer, *Nanoscale* **2014**, *6*, 24.
- [43] S. Nayak, I. J. McPherson, K. A. Vincent, *Angew. Chem., Int. Ed.* **2018**, *57*, 12855.
- [44] C. Tang, L. Chen, H. Li, L. Li, Y. Jiao, Y. Zheng, H. Xu, K. Davey, S. Qiao, *J. Am. Chem. Soc.* **2021**, *143*, 7819.
- [45] Y. Deng, L. Tang, C. Feng, G. Zeng, Z. Chen, J. Wang, H. Feng, B. Peng, Y. Liu, Y. Zhou, *Appl. Catal., B* **2018**, *235*, 225.
- [46] Y. Zhao, Y. Liu, Z. Wang, Y. Ma, Y. Zhou, X. Shi, Q. Wu, X. Wang, M. Shao, H. Huang, Y. Liu, Z. Kang, *Appl. Catal., B* **2021**, *289*, 120035.